Haptic rendering of rigid contacts using impulsive and penalty forces

Daniela Constantinescu, *Student Member, IEEE,* Septimiu E. Salcudean, *Member, IEEE,* and Elizabeth A. Croft, *Member, IEEE*

Abstract

A new simulation approach is proposed to improve the stability and the perceived rigidity of contacts during haptic interaction with multi rigid body virtual environments. The approach computes impulsive forces upon contact and penalty and friction forces during contact. The impulsive forces are derived using a new collision resolution method that never increases the kinetic energy of the system. When new contacts arise, the impulsive forces generate large hand accelerations without requiring increased contact stiffness and damping. Virtual objects and linkages are regarded as points in the configuration space and no distinction is made between them in the proposed approach.

Index Terms

Simultaneous collision resolution, multi rigid body simulation, haptic simulation, haptic rendering.

Manuscript received March 4, 2004; revised .

Regular paper

Corresponding author: D. Constantinescu is with the Robotics and Control Laboratory, University of British Columbia, Canada. Mailing address: Department of Electrical and Computer Engineering, 2356 Main Mall, UBC, Vancouver, B.C., Canada V6T 1Z4. Fax: (604) 822-5949. Email: danielac@ece.ubc.ca.

S. E. Salcudean is with the Robotics and Control Laboratory, University of British Columbia, Canada. Mailing address: Department of Electrical and Computer Engineering, 2356 Main Mall, UBC, Vancouver, B.C., Canada V6T 1Z4. Fax: (604) 822-5949. Email: tims@ece.ubc.ca.

E. A. Croft is with the Industrial Automation Laboratory, University of British Columbia, Canada. Mailing address: Department of Mechanical Engineering, 2054-2324 Main Mall, UBC, Vancouver, B.C., Canada V6T 1Z4. Fax: (604) 822-2403. Email: ecroft@mech.ubc.ca.

Haptic rendering of rigid contacts using impulsive and penalty forces

I. Introduction

In many virtual reality applications, haptic feedback is beneficial only if the forces rendered to users represent the physical phenomenon with sufficient accuracy. A main factor in enhancing the realism of the haptic manipulation of rigid objects and linkages is the perceived contact rigidity. As demonstrated by user studies [1], [2], the perceived rigidity of virtual contacts can be improved through applying large forces to users upon contact. A number of applications, such as virtual CAD prototyping or medical simulators for orthopedics, may benefit from improved perception of various levels of rigidity.

Both the virtual environment simulation and the haptic controller contribute to the perceived rigidity of the virtual contacts. The simulation computes interaction forces that reflect the employed model of rigid body contact and the controller transmits them to users. In existing haptics research, physically-based interactions within multi rigid body virtual environments are generated using three real time simulation methods developed in graphics and robotics: penalty-based, constraint-based, and impulse-based methods.

This research is concerned with improving the stability and the perceived rigidity of contacts during the haptic manipulation of virtual rigid objects and linkages. It proposes a simulation approach that combines constraint-based and penalty-based techniques. Specifically, it computes constraint-based impulsive forces upon contact and penalty-based and friction forces during contact. The impulsive forces are derived using a new rigid body contact model and a new pseudo-inverse based simultaneous collision resolution method that never increases the kinetic energy of the system[1]. A suitable controller transmits these forces to users.

The paper starts by reviewing relevant work in real time simulation, haptics simulation, and collision modeling, and by discussing the proposed approach in relation to this work. The new contact model is introduced in Section III, followed by the penalty-based second order dynamics of the virtual world in Section IV. In Section V, the dynamics used for collision resolution are derived from these second order dynamics. In addition, the new constraint-based simultaneous collision resolution method is shown to never increase the kinetic energy of the system. In Section VI, the haptic performance of the proposed approach is compared to that of the penalty-based and the constraint-based methods through simulations. Limitations imposed by the haptic device are discussed and solutions are devised to address them. Experiments are presented in Section VII. They demonstrate increased contact stability during user interaction with a planar virtual environment modeled by penalties and impulses compared to a penalties-alone model.

[1]Preliminary versions of this work were presented in [3] and [4].

II. Related work

In this section, real time multi rigid body simulation methods are overviewed. They are classified into penalty-based, constraint-based, and impulse-based techniques based on the model of rigid contact that they use. Each model recognizes different contact states and enforces constraint rigidity in a specific way. In particular, a colliding contact state is recognized only when constraints are modeled as perfectly rigid.

Penalty-based simulations recognize two contact states: no contact, if a positive separation distance exists between bodies; and resting contact, if bodies interpenetrate. Penalty-based methods approximate constraints by penalizing constraint violations proportional to the stiffness and the damping of the virtual contacts. General-purpose penalty-based algorithms [5] are computationally inexpensive and compatible with the fixed time step integrators required in haptics. They are used in many implementations, including in the haptic rendering of virtual worlds through a virtual tool [6]. However, the requirement for simulation stability limits the virtual contact damping [7]. In turn, the virtual damping limits the magnitude of the penalty-based forces that arise upon contact, and, hence, the perceived rigidity of the virtual world.

Constraint-based simulations recognize three contact states: no contact, if a positive separation distance exists between bodies; colliding contact, if the separation distance is zero and bodies move into each other at least at one contact; and resting contact, if the separation distance is zero and bodies maintain contact or move away from each other at all contacts. Constraint-based techniques enforce rigid constraints exactly and prevent body interpenetration by applying impulses at colliding contacts. Two types of algorithms implement constraint-based techniques. Event-driven schemes [8], [9] integrate the system dynamics between collision events, resolve occurring collisions, and reset the integrator before continuing to integrate the dynamics. Such algorithms are not directly useful in haptics because they require variable step size integrators, i.e., there is no guaranteed completion time. Time-stepping schemes [10], [11] solve a time-discretization of the system dynamics that includes the impact rules and the perfectly rigid constraints enforced at the velocity level. Such algorithms are compatible with fixed time steps, but have no guaranteed completion time. This is because they can avoid constraint drift only through accurate collision detection and the reformulation of the system dynamics at each contact configuration change. Since there exists no a priori bound on the number of collisions that can occur during one simulation step, the

computation time is unpredictable. Time-stepping simulations with constraint stabilization [12], [13], [14] have guaranteed completion time. However, these simulations were proven to not increase the kinetic energy of the system only for smooth convex objects undergoing perfectly plastic collisions [14]. Constraint-based methods developed for haptics [15], [16] model the colliding contacts between the user and the virtual world only implicitly and are compatible with fixed time step integrators. These methods are suitable for point interaction with virtual worlds, but their extension to rigid body interaction is not straightforward [17]. Moreover, the potential haptic advantage of perfectly rigid contacts is lost because the simulation does not compute constraint-based forces and impulses. Users perceive only penalty-like forces applied to them by the interaction controller.

Impulse-based simulations recognize two contact states: no contact, if a positive separation distance exists between bodies; and colliding contact, if the separation distance between bodies is zero. Impulse-based techniques [18] enforce rigid constraints exactly. They implement resting contact as a series of micro-collisions and apply impulses to prevent body interpenetration. Impulse-based techniques yield visually acceptable results, but haptically unconvincing resting contacts and dry friction [19]. Furthermore, the simulation becomes computationally intensive for frequent resting contacts [18].

Regardless of the technique used for generating the virtual environment, little haptics work exists that enhances the perception of rigidity through large force variations when new contacts arise. The earliest large force changes rendered to users upon contact are the "braking pulses" [20]. The braking pulses arise from a virtual wall model with high initial contact damping. They are designed to dissipate the entire kinetic energy of the user's hand during point interaction within virtual environments. Impulsive forces are used to model planar collisions of rigid bodies in [21] and of linkages in [22]. These forces satisfy Poisson's restitution hypothesis in a least squares sense and their passivity is not proven.

The approach proposed herein uses a new, impulse-augmented penalty contact model. Specifically, contacts are exactly enforced during collisions by impulses, and they are enforced only approximately otherwise by penalty functions. The approach maintains compatibility with fixed time step integrators by using penalty-based numerical methods during contact. At the same time, it improves the stability and the perceived rigidity of contacts by computing impulsive forces upon contact. The kinetic energy dissipated during collisions depends on the restitution properties and on the geometry of the contacts and is independent of the contact stiffness and damping. The approach generalizes earlier work in [20] in two ways: it allows the energy dissipated upon contact to be adjusted through the coefficient of restitution; and is suitable for rigid body simulation, as opposed to point interaction. Compared to earlier work in [21] and [22], it uses a new contact model and Newton's restitution hypothesis for collision resolution. The contact model allows transitions to the collision state from all contact states. Therefore, rigid body contact is represented more accurately (see Section III) and the simulation can account for device limitations (see Section VI). Newton's restitution hypothesis allows multiple collisions to be resolved such that the kinetic energy of the system never increases during collisions.

Compared to multi rigid body collision resolution methods developed in mechanics (see [23] for a comprehensive review of relevant work), the proposed technique sacrifices accuracy for computational efficiency. Accurate modeling of unilateral contacts requires the system dynamics to be derived based on the complementarity rule[2] and solved using numerical algorithms for complementarity problems, as in [24], [25], [10], [11], [14]. However, time-stepping complementarity formulations are computationally expensive for haptics (if they require constraint stabilization) or proven to not increase the system kinetic energy only for perfectly plastic collisions between smooth convex objects (if they include constraint stabilization). The complementarity formulation is sidestepped in the present approach by exactly enforcing rigid contacts only during collisions. Hence, collisions can be rendered to users through various high frequency force signals (as suggested in [26]) that dissipate the same amount of energy as the computed impulses. Such force signals may enable users to distinguish collisions between different materials (such as bone-bone, bone-metal, or metal-metal) and will be investigated in upcoming work. During collisions, three further simplifying assumptions are used in the present approach: (i) that impulses develop at all contacts at which bodies move into each other (while impulses may develop at only a subset of these contacts in the complementarity formulation); (ii) that velocities of all points in contact satisfy Newton's restitution law at contacts where impulses develop (while only their relative velocities obey Newton's hypothesis in the complementarity formulation); and (iii) that collisions are frictionless. These assumptions imply a particular choice of a multiple collision rule and sacrifice solution accuracy. However, they allow collision resolution to achieve the high fixed speed of the haptic controller.

III. The contact model

The proposed contact model is a dynamic model rather than a geometric one. It is used for computing interaction forces and impulses, based on the geometric information provided by a collision detection algorithm that is implemented in the virtual environment. Typically, the collision detection algorithm decomposes each rigid object into a collection of convex polyhedra and computes contacts between pairs of these polyhedra [27]. For each contact, it provides a contact point, a penetration depth, and a contact normal direction. In the present approach, a contact is defined by this geometric information plus the contact velocity. The contact velocity is the relative velocity between the contacting polyhedra at the contact point. It is defined such that the normal contact velocity (i.e., the component of the contact velocity along the contact

[2]In the normal contact direction, the rule states that either the relative displacement and relative velocity are zero and the constraint impulse is not zero or vice versa. In the contact plane, it states that either the tangential relative velocity is zero and the friction force is in the friction cone, or the relative tangential velocity is nonzero and the friction force is on the friction cone.

normal direction) is negative if the polyhedra move into each other.

As in [28], two rigid bodies are said to be in the same *contact group* if there exists a chain of contacting moving rigid bodies between them. The rigid body contact model proposed in this paper has three states (whose designation follows [29]): free motion, colliding contact, and resting contact. A rigid body is said to be in *free motion* if it has no contacts. A rigid body is said to be in *colliding contact* if at least one new contact with negative normal contact velocity exists within its contact group. Finally, a rigid body is said to be in *resting contact* if it is neither in free motion nor in colliding contact (i.e., the body can have non-zero acceleration and velocity during resting contact). In a haptic simulation, bodies may remain in colliding contact for multiple consecutive simulation steps because new contacts may appear at every step.

The collision state of the proposed rigid body contact model is introduced to emphasize new contacts. However, used in direct conjunction with typical collision detection algorithms, the model may emphasize numerical artifacts rather than physical phenomena. Consider, for example, the case of a virtual ball-socket joint. Depending on the object representation used for collision detection, either a polyhedron with a large number of faces approximates the ball and a large number of convex polyhedra compose the concave socket, or several trimmed NURBS approximate the ball and the socket. Furthermore, body contact is represented through a finite number of contacts between the convex pieces composing the ball and the socket. When the ball rolls in the socket and the convex pieces in contact change, most collision detection algorithms fail to maintain contact continuity and report a large number of easily forming and breaking contacts. If these contacts are used directly in the proposed rigid body contact model, the ball-socket joint will frequently switch to colliding contact instead of maintaining resting contact. Unless this artifact is eliminated, it will be emphasized by the proposed rigid body contact model (as well as by any other contact model that distinguishes a collision state upon contact) and the realism of the interaction may be destroyed.

Two steps are used in the present approach to eliminate this numerical artifact. First, sufficiently close contacts are collapsed into a single contact using clustering [27]. Second, the temporal coherence of the remaining contacts is maintained using spatial coherence. In other words, contacts existing at two consecutive time steps are considered the same contact if they are within a pre-specified distance of each other. Time coherence breaks down if the virtual objects move more than the pre-specified distance during one simulation step. Therefore, this distance must be chosen based on the maximum speed of the virtual object motion and the time step of the simulation.

The proposed rigid body contact model combines approximate and exact constraint enforcement during resting and colliding contact, respectively. Hence, it requires penalty-based resting contact dynamics and constraint-based collision resolution. The numerical methods used to resolve resting contact dynamics are presented in the next section. The proposed multiple collision resolution technique follows in Section V.

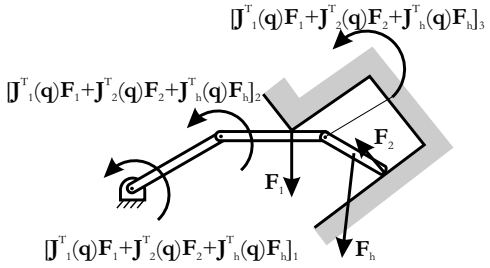

Fig. 1. Example contact and hand forces arising during the haptic manipulation of a contact group with dynamics computed in configuration space.

IV. RESTING CONTACT

This work considers the case in which users manipulate both virtual objects and virtual linkages (called virtual tools hereafter). Realistic forces during these types of interaction can be computed by representing the virtual world dynamics in either Cartesian space or in configuration space. In Cartesian space, a number of constraint equations must be added to maintain the bilateral constraints and the simulation must integrate a computationally expensive differential algebraic system of equations for which constraint satisfaction may be problematic [9]. In configuration space, the bilateral constraints are embedded in the coordinate representation. In this case, only a reduced number of coordinates must be integrated and bilateral constraint satisfaction is guaranteed. Virtual objects and virtual linkages become points evolving in this space and are indistinguishable. Therefore, configuration space dynamics are used in the proposed simulation to compute the interactions between the user and the virtual world.

Since bilateral constraints are incorporated in the coordinate representation, only contact and user applied forces must be included in the dynamics equations. Consider a contact group with d degrees of freedom (DOF) and c resting contacts. In configuration space, its dynamics [3] are:

$$\boldsymbol{D}(\boldsymbol{q})\,\ddot{\boldsymbol{q}} + \boldsymbol{B}(\boldsymbol{q},\dot{\boldsymbol{q}}) + \boldsymbol{G}(\boldsymbol{q}) = \sum_{i=1}^{c} \boldsymbol{J}_i^T(\boldsymbol{q})\,\boldsymbol{F}_i + \boldsymbol{J}_h^T(\boldsymbol{q})\,\boldsymbol{F}_h. \tag{1}$$

In (1), $\boldsymbol{D}(\boldsymbol{q}) \in \mathcal{R}^{d\times d}$ is the configuration space inertia matrix of the contact group, $\boldsymbol{B}(\boldsymbol{q},\dot{\boldsymbol{q}}) \in \mathcal{R}^{d}$ represent Coriolis and centripetal effects, $\boldsymbol{G}(\boldsymbol{q}) \in \mathcal{R}^{d}$ are the gravitational terms, $\boldsymbol{J}_i(\boldsymbol{q}) \in \mathcal{R}^{d\times 3}$ is the manipulator Jacobian computed at the i-th contact, $\boldsymbol{F}_i \in \mathcal{R}^3$ is the Cartesian space contact force at the i-th contact, $\boldsymbol{J}_h(\boldsymbol{q}) \in \mathcal{R}^{d\times 6}$ is the manipulator Jacobian computed at the user's hand, $\boldsymbol{F}_h \in \mathcal{R}^6$ is the Cartesian space generalized force (force and torque) applied by the user, and $\boldsymbol{q} \in \mathcal{R}^d$, $\dot{\boldsymbol{q}} \in \mathcal{R}^d$, and $\ddot{\boldsymbol{q}} \in \mathcal{R}^d$ are the configuration space positions, velocities, and accelerations, respectively (see Figure 1).

If the contact group consists of both virtual objects and virtual linkages, the matrices and vectors in (1) are obtained by concatenating the matrices and vectors corresponding to

[3]Note that the implementation of (1) limits the complexity of the linkages that can be manipulated. However, it does not limit users' ability to manipulate linkages using the proposed approach.

each object and linkage. For example:

$$\boldsymbol{q}^T = \begin{pmatrix} \boldsymbol{q}_1 & \cdots & \boldsymbol{q}_m \end{pmatrix} \tag{2}$$

and:

$$\boldsymbol{D}(\boldsymbol{q}) = \begin{bmatrix} \boldsymbol{D}_1(\boldsymbol{q}_1) & \cdots & \boldsymbol{0} \\ \vdots & & \\ \boldsymbol{0} & \cdots & \boldsymbol{D}_m(\boldsymbol{q_m}) \end{bmatrix}. \tag{3}$$

In (3), m is the total number of virtual objects and virtual linkages and the configuration space dynamics of a virtual rigid body are the same as its Cartesian space dynamics.

The contact forces in (1) have a component $F_{n,i}$ along the contact normal direction $\boldsymbol{n}_i$, modeling contact rigidity, and a component $F_{f,i}$ along the direction $\boldsymbol{t}_i$ (orthogonal to the contact normal), modeling dry friction:

$$\boldsymbol{F}_i = F_{n,i}\boldsymbol{n}_i + F_{f,i}\boldsymbol{t}_i. \tag{4}$$

In the proposed approach, resting contact is enforced using penalties. Hence, the normal component of the contact force at the i-th contact is computed by:

$$F_{n,i} = -K_{contact}s_i(\boldsymbol{q}) - B_{contact}v_{n,i}(\boldsymbol{q}). \tag{5}$$

In (5), $K_{contact}$ and $B_{contact}$ are the contact stiffness and damping, s_i is the separation between bodies at contact (because bodies overlap, s_i is negative and equal to the penetration depth of the contact), and $v_{n,i}$ is the normal contact velocity. Dry friction is modeled using a modified Coulomb model. Hence, the tangential component of the contact force at the i-th contact is computed by:

$$F_{f,i} = \begin{cases} \mu F_{n,i} & \text{if} \quad |v_{t,i}| \geq v_{threshold} \\ \frac{v_{t,i}}{v_{threshold}}\mu F_{n,i} & \text{otherwise} \end{cases}. \tag{6}$$

In (6), μ is the coefficient of dry friction for the pair of contacting bodies and $v_{t,i}$ is the tangential contact velocity (the component of the contact velocity orthogonal to the contact normal direction). The threshold value $v_{threshold}$ allows the contact to transition between the stick and the slip friction states. Any friction model that employs only vertex contact state information can replace the model in (6), such as [30] or [31].

As shown by (5) and (6), only state information is used in the proposed simulation to compute contact forces. Therefore, (1) can be directly solved for the configuration space acceleration:

$$\ddot{\boldsymbol{q}} = \boldsymbol{D}^{-1}\left(\sum_{i=1}^{c}\boldsymbol{J}_i^T\boldsymbol{F}_i + \boldsymbol{J}_h^T\boldsymbol{F}_h - \boldsymbol{B} - \boldsymbol{G}\right). \tag{7}$$

In (7), the dependence on the instantaneous state of all terms on the right hand side of the equation is implied. The configuration space acceleration is then integrated using a fixed step size integrator compatible with the requirements of the haptic control loop.

While the resting contact dynamics discussed in this section are typical for penalty-based simulations, the dynamics of colliding contact implement a constraint-based approach. These dynamics are presented in the next section.

V. Collision resolution

The colliding contact state is introduced in the proposed approach to improve the penalty-based approximation of unyielding contacts. In conjunction with the fixed step size of the haptic simulation, this state requires multiple collisions to be resolved simultaneously. Rather than incorporating contact rigidity and dry friction into a complementarity formulation, the proposed approach uses three simplifying assumptions: (i) that impulses develop at all contacts at which bodies move into each other during a collision; (ii) that velocities of all points in contact obey Newton's restitution law at contacts at which impulses develop; and (iii) that collisions are frictionless. Unlike more accurate multiple collision models [24], [32], [25], this new technique is non-iterative. This is advantageous in haptics, because of the hard limits imposed by the force controller on computation times. Unlike the model in [14], it makes no assumption about the coefficient of restitution or the shape of the colliding objects.

The colliding contact dynamics are obtained through time integration of (1):

$$\boldsymbol{D}\dot{\boldsymbol{q}} = \boldsymbol{D}\dot{\boldsymbol{q}}_0 + \sum_{i=1}^{c}\int_{t_0}^{t}\boldsymbol{J}_i^T\boldsymbol{F}_i dt = \boldsymbol{D}\dot{\boldsymbol{q}}_0 + \sum_{i=1}^{c}\boldsymbol{J}_i^T\boldsymbol{p}_i. \tag{8}$$

In (8), $\boldsymbol{D}\dot{\boldsymbol{q}}_0$ and $\boldsymbol{D}\dot{\boldsymbol{q}}$ are the pre- and post-collision configuration space momenta and $\boldsymbol{p}_i = \int_{t_0}^{t}\boldsymbol{F}_i dt$ is the i-th contact impulse. Since the collision is modeled as an instantaneous event, i.e., $t \to t_0$, the hand and gravitational forces do not contribute impulses to the impulse and momentum balance of the system. Furthermore, apart from the collision impulses, no other external impulses are applied to the contact group.

In addition, collisions are assumed frictionless, i.e., $\boldsymbol{p}_i = p_i\boldsymbol{n}_i$, with p_i being the magnitude of the i-th contact impulse. Then, the configuration space dynamics of colliding contact become:

$$\boldsymbol{D}\dot{\boldsymbol{q}} = \boldsymbol{D}\dot{\boldsymbol{q}}_0 + \sum_{i=1}^{c}\boldsymbol{J}_i^T\boldsymbol{n}_i p_i = \boldsymbol{D}\dot{\boldsymbol{q}}_0 + \boldsymbol{\mathcal{J}}_c^T\boldsymbol{p}. \tag{9}$$

In (9), $\boldsymbol{p} = \begin{pmatrix} p_1 \dots p_i \dots p_c \end{pmatrix}^T$ is the vector of contact impulses and $\boldsymbol{\mathcal{J}}_c = \begin{bmatrix} \boldsymbol{J}_1^T\boldsymbol{n}_1 \dots \boldsymbol{J}_i^T\boldsymbol{n}_i \dots \boldsymbol{J}_c^T\boldsymbol{n}_c \end{bmatrix}^T$. For a contact group with d DOF and c colliding contacts, (9) represents a set of d equations with $d + c$ unknowns, the post-collision configuration space velocity $\dot{\boldsymbol{q}}$ and the contact impulses $\boldsymbol{p}$. Further assumptions are needed to solve such a system [23]. These assumptions are provided by the various collision laws proposed in the literature [24], [32], or [25]. To allow the development of a non-iterative solution, Newton's restitution hypothesis is used in this work. Furthermore, the method is proven to never increase the kinetic energy of the contact group.

For one colliding contact, Newton's restitution hypothesis relates the pre-collision (v_{n0}) and post-collision (v_n) normal contact velocities through the coefficient of restitution e:

$$v_n = -ev_{n0}. \tag{10}$$

The coefficient of restitution $e \in \begin{bmatrix} 0,1 \end{bmatrix}$ describes the nature of the collision, with $e = 1$ corresponding to a perfectly

elastic collision (no energy loss), and $e = 0$ corresponding to a perfectly plastic collision.

In configuration space, (10) becomes:

$$\boldsymbol{n}^T \boldsymbol{J}_{b_i} \boldsymbol{q} = -e \boldsymbol{n}^T \boldsymbol{J}_{b_i} \boldsymbol{q}_0 \tag{11}$$

at a collision between body b_i of the contact group and a static environment, and:

$$\boldsymbol{n}^T \left(\boldsymbol{J}_{b_i} - \boldsymbol{J}_{b_j} \right) \boldsymbol{q} = -e \boldsymbol{n}^T \left(\boldsymbol{J}_{b_i} - \boldsymbol{J}_{b_j} \right) \boldsymbol{q}_0 \tag{12}$$

at a self-collision, i.e., a collision between bodies b_i and b_j of the contact group. A more restrictive condition is imposed at a self-collision in the proposed approach. Namely, the second simplifying assumption is imposed on the contact group by requiring it to obey:

$$\boldsymbol{n}^T \boldsymbol{J}_{b_i} \boldsymbol{q} = -e \boldsymbol{n}^T \boldsymbol{J}_{b_i} \boldsymbol{q}_0 \tag{13}$$

and:

$$\boldsymbol{n}^T \boldsymbol{J}_{b_j} \boldsymbol{q} = -e \boldsymbol{n}^T \boldsymbol{J}_{b_j} \boldsymbol{q}_0 \tag{14}$$

simultaneously. (13) and (14) ensure both that Newton's restitution law is observed and that the proposed collision resolution technique maintains system passivity, as shown in subsequent derivations. Using Equations (11), (13), and (14), Newton's restitution law is restated as:

$$\boldsymbol{\mathcal{J}}_c \dot{\boldsymbol{q}} = -e \boldsymbol{\mathcal{J}}_c \dot{\boldsymbol{q}}_0. \tag{15}$$

(15) represents a set of c equations, where self-collisions are counted once on each colliding body. Note also that the equal sign in (15) embeds the first simplifying assumption used in this work for resolving collisions.

In the proposed simulation method, (9) and (15) describe the dynamics of colliding contact of a contact group with d DOF and c simultaneous collisions. Their resolution and the proof of the system passivity for both independent and overdetermined constraints are presented next, followed by the technique used to render collisions to users.

A. Independent constraints

This section starts by showing that a contact group with one frictionless contact is passive if its colliding contact dynamics are resolved using Newton's hypothesis. The result is then extended to a contact group with multiple independent contacts for which (15) is used to ensure that Newton's collision law is obeyed.

Passivity of a contact group with a single colliding contact is shown by proving that:

Theorem 1: If a contact group described by the momentum equation:

$$\boldsymbol{D} \dot{\boldsymbol{q}} = \boldsymbol{D} \dot{\boldsymbol{q}}_0 + \boldsymbol{\mathcal{J}}_c^T \boldsymbol{p}$$

has one frictionless colliding contact and the post-collision normal contact velocity is given by:

$$v_n = -e v_{n0},$$

where $e \in [0,1]$ is the coefficient of restitution, then the post-collision kinetic energy of the contact group is:

$$KE = KE_0 - \left(1 - e^2\right) \dot{\boldsymbol{q}}_0^T \boldsymbol{\mathcal{J}}_c^T \overline{\boldsymbol{\mathcal{J}}}_c^T \boldsymbol{D} \overline{\boldsymbol{\mathcal{J}}}_c \boldsymbol{\mathcal{J}}_c \dot{\boldsymbol{q}}_0 \leq KE_0 \tag{18}$$

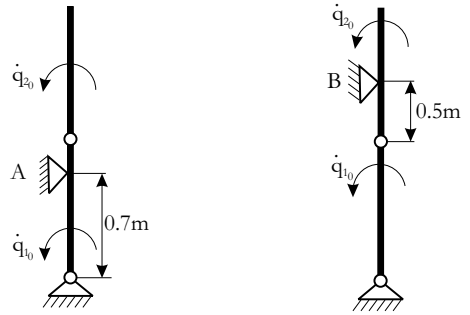

(a) Collision at A. (b) Collision at B.

Fig. 2. Two link planar manipulator whose loss of kinetic energy for various values of the coefficient of restitution is shown in Figure 3 for two different contact geometries.

where $\overline{\boldsymbol{\mathcal{J}}}_c = \boldsymbol{D}^{-1} \boldsymbol{\mathcal{J}}_c^T \left(\boldsymbol{\mathcal{J}}_c \boldsymbol{D}^{-1} \boldsymbol{\mathcal{J}}_c^T \right)^{-1}$ is the dynamically consistent inverse of $\boldsymbol{\mathcal{J}}_c$ [33].

The proof of Theorem 1 is presented in Appendix I.

Notes:

As shown in Appendix I, the contact impulse due to one collision is:

$$\boldsymbol{p} = -\left(1 + e\right) \left(\boldsymbol{\mathcal{J}}_c \boldsymbol{D}^{-1} \boldsymbol{\mathcal{J}}_c^T \right)^{-1} \boldsymbol{\mathcal{J}}_c \dot{\boldsymbol{q}}_0. \tag{19}$$

This impulse is equal to the contact impulse computed in prior complementarity formulations [24]. Hence, the simplifying assumptions embedded in (15) involve no further approximation for the case of a single colliding contact. Moreover, the proposed collision resolution method uses the dynamically consistent inverse of the collision Jacobian, i.e., it is coordinate invariant.

Kinetic energy is conserved during a perfectly elastic collision ($e = 1$). The loss of kinetic energy during a plastic collision ($e < 1$) depends both on contact properties, as given by the coefficient of restitution e, and on contact geometry and the contact group topology and geometry, embedded in $\boldsymbol{\mathcal{J}}_c$. For example, various contact group topologies and geometries and various contact geometries result in either a total or a partial loss of kinetic energy during a plastic collision. Two examples of how the loss of kinetic energy during a frictionless collision varies with the coefficient of restitution are depicted in Figure 3 for two different contact geometries of the two link planar manipulator depicted in Figure 2. The manipulator has link lengths $l_1 = l_2 = 1$m, link masses $m_1 = m_2 = 1$kg, configuration space position $\boldsymbol{q} = \begin{pmatrix} \frac{\pi}{2} & 0 \end{pmatrix}^T$rad, and pre-collision configuration space velocity $\dot{\boldsymbol{q}}_0 = \begin{pmatrix} 1 & 1 \end{pmatrix}^T$rad/s.

The collision resolution method employed for one colliding contact can be directly applied to resolve multiple collisions simultaneously if the contact constraints are independent, i.e., $\boldsymbol{\mathcal{J}}_c$ is full row rank, and (15) is imposed to ensure that the post-collision configuration space velocity obeys Newton's hypothesis. Then, $\boldsymbol{\mathcal{J}}_c$ is full row rank and the matrix $\boldsymbol{\mathcal{J}}_c \boldsymbol{D}^{-1} \boldsymbol{\mathcal{J}}_c^T$

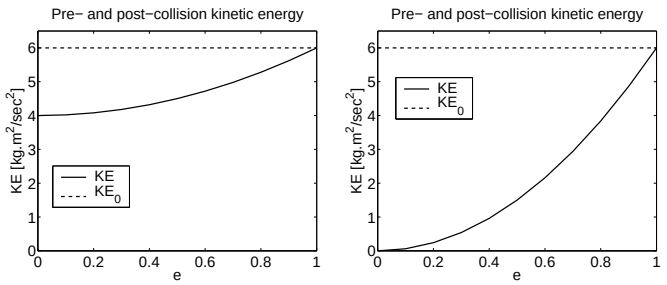

(a) Collision at A. (b) Collision at B.

Fig. 3. Loss of kinetic energy of the planar two link manipulator in Figure 2 during one frictionless collision for two different contact geometries.

is invertible (see the Appendix for proof).

B. Overdetermined constraints

If the contact constraints are overdetermined, $\boldsymbol{\mathcal{J}}_c$ is rank deficient and the matrix $\boldsymbol{\mathcal{J}}_c \boldsymbol{D}^{-1} \boldsymbol{\mathcal{J}}_c^T$ is not invertible. Nevertheless, its pseudo-inverse $\left(\boldsymbol{\mathcal{J}}_c \boldsymbol{D}^{-1} \boldsymbol{\mathcal{J}}_c^T\right)^\dagger$ can be used to compute the contact impulses, and the post-collision configuration space velocity according to:

$$\boldsymbol{p} = -(1+e)\left(\boldsymbol{\mathcal{J}}_c \boldsymbol{D}^{-1} \boldsymbol{\mathcal{J}}_c^T\right)^\dagger \boldsymbol{\mathcal{J}}_c \dot{\boldsymbol{q}}_0 \quad (20)$$

$$\dot{\boldsymbol{q}} = \dot{\boldsymbol{q}}_0 - (1+e)\,\boldsymbol{D}^{-1} \boldsymbol{\mathcal{J}}_c^T \left(\boldsymbol{\mathcal{J}}_c \boldsymbol{D}^{-1} \boldsymbol{\mathcal{J}}_c^T\right)^\dagger \boldsymbol{\mathcal{J}}_c \dot{\boldsymbol{q}}_0. \quad (21)$$

Passivity of a contact group with overdetermined colliding constraints resolved simultaneously according to (21) results from the following theorem:

Theorem 2: If a contact group described by the momentum equation:

$$\boldsymbol{D}\dot{\boldsymbol{q}} = \boldsymbol{D}\dot{\boldsymbol{q}}_0 + \boldsymbol{\mathcal{J}}_c^T \boldsymbol{p},$$

has c overdetermined frictionless colliding contacts and its post-collision configuration space velocity is given by:

$$\boldsymbol{\mathcal{J}}_c \dot{\boldsymbol{q}} = -e\boldsymbol{\mathcal{J}}_c \dot{\boldsymbol{q}},$$

where $e \in [0,1]$ is the coefficient of restitution, then the post-collision kinetic energy of the contact group is:

$$KE = KE_0 - \left(1-e^2\right) \dot{\boldsymbol{q}}_0^T \boldsymbol{\mathcal{J}}_n^T \overline{\boldsymbol{\mathcal{J}}}_n^T \boldsymbol{D} \overline{\boldsymbol{\mathcal{J}}}_n \boldsymbol{\mathcal{J}}_n \dot{\boldsymbol{q}}_0 \leq KE_0. \quad (24)$$

In (24), $\overline{\boldsymbol{\mathcal{J}}}_n = \boldsymbol{D}^{-1} \boldsymbol{\mathcal{J}}_n^T \left(\boldsymbol{\mathcal{J}}_n \boldsymbol{D}^{-1} \boldsymbol{\mathcal{J}}_n^T\right)^{-1}$ is the dynamically consistent inverse of $\boldsymbol{\mathcal{J}}_n$, and $\boldsymbol{\mathcal{J}}_c^T = \begin{bmatrix}\boldsymbol{\mathcal{J}}_n^T & \boldsymbol{\mathcal{J}}_r^T\end{bmatrix}^T$ with $\boldsymbol{\mathcal{J}}_n$ full row rank.

The proof of Theorem 2 is presented in Appendix II.

Notes:

Similar to the case of independent constraints, the loss of kinetic energy depends both on contact properties, through the coefficient of restitution e, and on contact group topology and geometry and contact geometry, through $\boldsymbol{\mathcal{J}}_n$. Kinetic energy is conserved during perfectly elastic collisions ($e = 1$).

From (33), it also follows that:

$$\dot{\boldsymbol{q}} = \dot{\boldsymbol{q}}_0 - (1+e)\,\boldsymbol{D}^{-1} \boldsymbol{\mathcal{J}}_c^T \left(\boldsymbol{\mathcal{J}}_c \boldsymbol{D}^{-1} \boldsymbol{\mathcal{J}}_c^T\right)^\dagger \boldsymbol{\mathcal{J}}_c \dot{\boldsymbol{q}}_0 = \\ = \dot{\boldsymbol{q}}_0 - (1+e)\,\boldsymbol{D}^{-1} \boldsymbol{\mathcal{J}}_n^T \left(\boldsymbol{\mathcal{J}}_n \boldsymbol{D}^{-1} \boldsymbol{\mathcal{J}}_n^T\right)^{-1} \boldsymbol{\mathcal{J}}_n \dot{\boldsymbol{q}}_0 \quad (25)$$

In other words, the post-collision state of the contact group is the same regardless whether the collisions are resolved using the pseudo-inverse technique or constraint overdeterminancy is eliminated before collision resolution. Hence, the pseudo-inverse method is equivalent to selecting a set of independent constraints and simultaneously resolving the collisions at these contacts as described in Section V-A.

C. Rendering collisions to the user

The contact impulses are rendered to the user as impulsive forces through a four channel teleoperation controller [34]. The configuration space impulsive forces to be applied to the user's hand are computed such that they induce the same change in the configuration space momentum of the contact group when integrated over one time step of the haptic simulation:

$$\boldsymbol{F}_{env} = \frac{\boldsymbol{\mathcal{J}}_c^T \boldsymbol{p}}{\Delta t}. \quad (26)$$

In (26), Δt is the haptic time step and $\boldsymbol{p}$ are the contact impulses, computed according to (19) and (20).

VI. Simulations

In this section, the performance of the proposed simulation approach is compared to the performance of the penalty-based and constraint-based approaches through simulation of user interaction within a planar virtual environment. The limitations of the haptic device are considered and a solution is proposed to address them.

Note that, although suitable for rigid body interaction within spatial virtual environments, the impulse-augmented penalty-based approach is validated only for 3 DOF (x, y, θ) rigid body interaction within a planar virtual world in the present work. This is due to the availability of only planar (F_x, F_y, τ_z) and point (F_x, F_y, F_z) haptic interaction systems in the Robotics and Control Laboratory. Interfaces without torque feedback (such as 3 DOF point interaction devices) are unsuitable for implementing the proposed approach. A device such as the Phantom Premium 6DOF, with full torque feedback would be necessary. To guarantee that the kinetic energy of the user's hand will not increase during collisions as a result of the impulsive feedback, full rigid body force and torque feedback is required (F_x, F_y, τ_z during planar interaction and F_x, F_y, F_z, τ_x, τ_y, τ_z during spatial interaction). Unstable interaction may arise due to the lack of torque feedback.

Figure 4 depicts the virtual environment employed in the simulations. Users manipulate a rectangular peg by applying forces and torques at its center of mass. The virtual world is connected to the haptic interface through a unilateral coupler [15], [9] when generated using a constraint-based approach, and through a four-channel teleoperation controller [34] when generated using the proposed and the penalty-based approaches. The unilateral coupler extends to

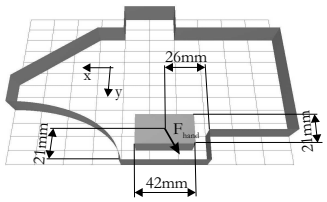

Fig. 4. Planar virtual world used in simulations and experiments. Starting from rest and the position shown, the rectangular object is pushed into the lower right corner by a controlled constant force.

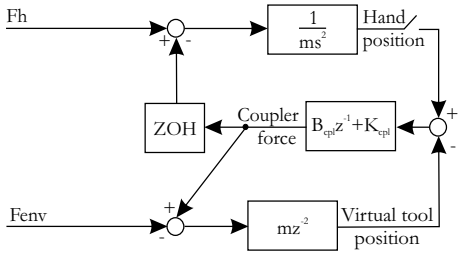

(a) Simulink diagram of the unilateral coupler.

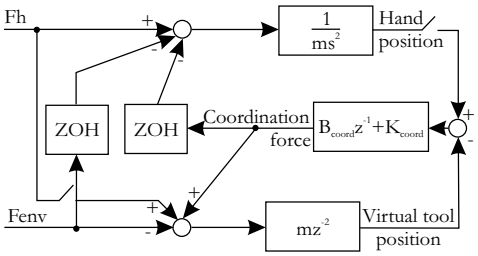

(b) Simulink diagram of the four channel controller.

Fig. 5. Simulink diagrams of the controllers connecting the haptic device and the virtual environment. Controller parameters are given in Table I.

rigid body interaction the controller used in the god-object [15] and the virtual proxy [9] point interaction techniques[4]. It is a proportional derivative (PD) controller that coordinates the positions of the device and the virtual tool during constrained motion (Figure 5(a)). The unilateral coupler is inactive during free motion. Hence, it acts as two unilateral spring-damper pairs between the device and the virtual tool, one translational and one rotational. The teleoperation controller (Figure 5(b)) has two position channels and two force channels. The two position coordination channels form a PD controller that acts as two spring-damper pairs (one translational and one rotational) between the device and the virtual tool. The two force channels are used to apply the hand force F_h to the virtual tool and the environment force F_{env} to the user's hand.

In the simulations, the user pushes the virtual peg towards

[4]However, since it is not clear how the god-object and the virtual proxy simulations can be extended to rigid body interaction, the virtual world is evolved using forward dynamics algorithms similar to those developed in graphics [8].

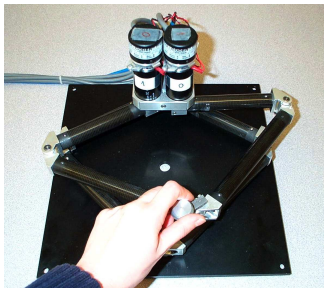

Fig. 6. The impedance device modeled in the simulations in this section and employed in the experiments described in Section VII.

the corner with a force $\boldsymbol{F}_h = \begin{pmatrix} -0.32\text{N} & 0.4\text{N} & 0\text{Nm} \end{pmatrix}^T$. This simple interaction is chosen to illustrate the proposed approach both because it can be validated experimentally and because the constraints are overdetermined. The peg has dimensions $l_1 = 0.021$m and $l_2 = 0.0105$m, mass $m = 2$kg, and moment of inertia $I = 0.005\text{kgm}^2$. The virtual walls have stiffness $K_{wall} = 1000$N/m and damping $B_{wall} = 50$N/(m/s). Collisions are considered perfectly plastic ($e = 0$). The stiffness and damping of the position coordination channels of the teleoperation controller connecting the proposed and the penalty-based virtual environments and of the unilateral coupler connecting the constraint-based virtual world to the device are given in Table I. The parameters of the teleoperation controller are optimized for transparency [34], while those of the unilateral coupler are chosen to match the impedance of the virtual contacts. To match the planar interface used for experiments, the haptic device is modeled as an impedance device. Furthermore, it is considered to have purely inertial dynamics and to be kinematically equivalent to the proxy, i.e., the local device controller is not modeled. The user's hand is modeled as a pure force source, which is a worst-case scenario for stability when an impedance device is used [35] (see Figure 6 for a photo of the impedance device used in the experiments described in Section VII and modeled in the simulations in this section).

In the first set of simulations, it is assumed that the device actuators can apply the impulse-augmented penalty interactions computed by the proposed simulation and reflected to the device by the four channel teleoperation controller. The resulting hand trajectories are depicted in Figure 7 and the forces that would be felt by the user are shown in Figure 8. Figure 7 demonstrates that the hand trajectory is closer to the ideal hand trajectory when users interact with a world generated using the proposed approach than when they interact with a penalty-based or a constraint-based virtual environment. The user-perceived forces are closer to the ideal forces, too. Users feel large forces when new contacts arise (see Figure 8), and they feel forces that only balance the low hand force $\boldsymbol{F}_h = \begin{pmatrix} -0.32\text{N} & 0.4\text{N} & 0\text{Nm} \end{pmatrix}^T$ during contact. Note that while the large impulsive forces improve the perception of rigidity [1], [2], they may exceed the force capabilities of the device.

Several techniques can be used to account for the limitations of the haptic interface in the proposed approach:

TABLE I

STIFFNESS AND DAMPING OF THE COORDINATION CONTROLLER AND THE UNILATERAL COUPLER CONNECTING THE VIRTUAL ENVIRONMENT TO THE HAPTIC INTERFACE.

Four channel Controller	**Unilateral coupler**
$\boldsymbol{K}_{coord} = \begin{pmatrix}100\text{N/m} & 100\text{N/m} & 0.5\text{N/rad}\end{pmatrix}^T$	$\boldsymbol{K}_{cpl} = \begin{pmatrix}1000\text{N/m} & 1000\text{N/m} & 2.5\text{N/rad}\end{pmatrix}^T$
$\boldsymbol{B}_{coord} = \begin{pmatrix}70\text{N/(m/s)} & 70\text{N/(m/s)} & 0.375\text{N/(rad/s)}\end{pmatrix}^T$	$\boldsymbol{B}_{cpl} = \begin{pmatrix}50\text{N/(m/s)} & 50\text{N/(m/s)} & 0.125\text{N/(rad/s)}\end{pmatrix}^T$

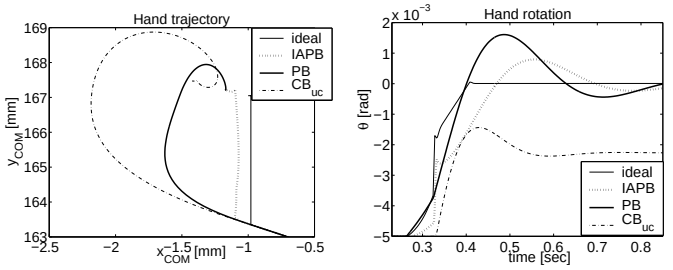

(a) (b)

Fig. 7. Simulated hand trajectories obtained when constraint-based ("ideal"), impulse-augmented penalty-based ("IAPB"), and penalty-based ("PB") interactions are transmitted to users by the four channel controller, and when constraint-based interactions are transmitted by the unilateral coupler ("CB_{uc}"). The device applies the simulated impulses to users in one step. Note that the hand trajectory is closest to the ideal trajectory when the virtual world is generated using the proposed approach and the simulated forces are transmitted to users by a four channel controller.

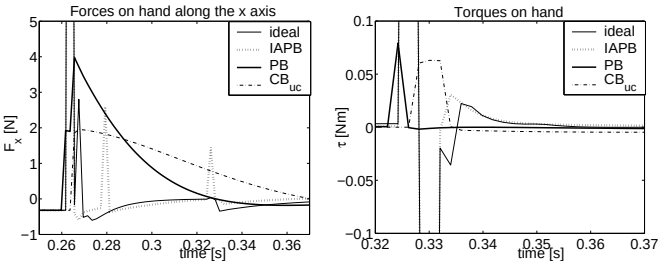

(a) (b)

Fig. 8. Simulated forces along the x-axis and torques applied to users by the four channel controller when the virtual world is generated using the constraint-based ("ideal"), the impulse-augmented penalty-based ("IAPB"), and the penalty-based ("PB") methods, and applied by the unilateral coupler when the virtual environment is generated using the constraint-based method ("CB_{uc}"). The device applies the simulated impulses to users in one step. Note the large collision impulses applied to users by the four channel controller when the virtual world is generated using the proposed approach.

- Collision impulses can be saturated on the device. When this strategy is used, the simulation computes collision impulses according to (20) and sends them to the four channel controller according to (26). The controller then saturates the impulses to the maximum value that the actuators can apply to the device. Hence, full collision impulses are applied to the virtual tool in the simulation and saturated impulses are applied to the device. As a result, different amounts of kinetic energy are extracted from the virtual tool and the device during collision and the kinematic correspondence between the two can be changed significantly, depending on the system dynamics. Post-collision kinematic correspondence is re-established through the position coordination channel of the four channel controller. This channel is much more compliant than the contact.
- Collision impulses can be scaled in the simulation. When this strategy is used, the simulation computes collision impulses according to (20) and scales them to the maximum value achievable through device actuation. The scaled impulses are applied to the virtual tool and sent to the four channel controller. As a result, the same amount of kinetic energy is extracted from the virtual tool and the device during collision and their kinematic correspondence is maintained, but the simulation is altered.
- Collision impulses can be spread over several steps of the simulation. When this strategy is used, the simulation scales the collision impulses as explained above. However, the colliding bodies do not transition to resting contact if scaling is necessary. Rather, they transition back to colliding contact and new collision impulses are computed at each step of the simulation until the force levels return to the range of the haptic device. As a result, the amount of kinetic energy extracted from the virtual tool and the device at each simulation step is the maximum allowable by the actuators, while the amount extracted over several steps is equal to that prescribed by (24). Furthermore, the kinematic correspondence between the virtual tool and the device is preserved.

Simulated hand trajectories obtained by using these techniques (assuming that the maximum force capability of the device is $\boldsymbol{F}_{limit} = \begin{pmatrix}15\text{N} & 15\text{N} & 1\text{Nm}\end{pmatrix}^T$) are presented in Figure 9. In this figure, "p_{full}" is the trajectory obtained when the device can fully apply the simulated collision impulses, "$\text{p}_{saturated}$" is obtained when collision impulses are saturated on the device, "p_{scaled}" is obtained when collision impulses are scaled in the virtual environment, and "p_{spread}" is obtained when collision impulses are spread over several steps of the simulation. The hand trajectory degrades as the force capabilities of the device decrease. The loss of performance is highest if the interaction forces are saturated on the device. In this case, full collision impulses are applied to the virtual tool which stops abruptly and only limited forces are applied to the user's hand, which continues to move. After collision, the user's hand is coordinated with the virtual tool through the four channel teleoperation controller, whose stiffness $\boldsymbol{K}_{coord}$ and damping $\boldsymbol{B}_{coord}$ are much lower than those of the virtual walls, K_{wall} and B_{wall}. Hence, constraint violation is largest and settling time increases (transient response is poorest). The

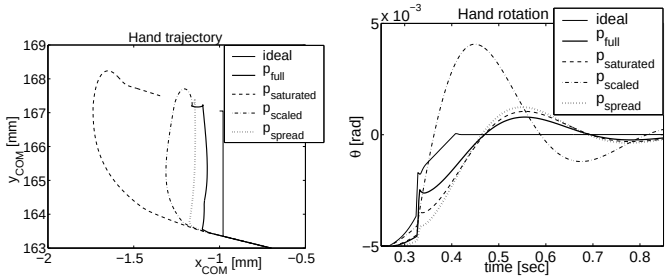

(a) (b)

Fig. 9. Simulated hand trajectories during user interaction with the impulse-augmented penalty-based virtual world when the device limitations are ignored and when they are taken into account ("ideal" - full constraint-based collision impulses are applied to users; "p_{full}" - full collision impulses are applied to users; "$\mathrm{p}_{saturated}$" - collision impulses are saturated on the device; "p_{scaled}" - collision impulses are scaled in the virtual environment; "p_{spread}" - collision impulses are spread over several simulation steps when necessary). Note that device limitations are overcome best by spreading the collision impulses over several time steps. Hence, this is the technique used to address device limitations in subsequent simulations and experiments.

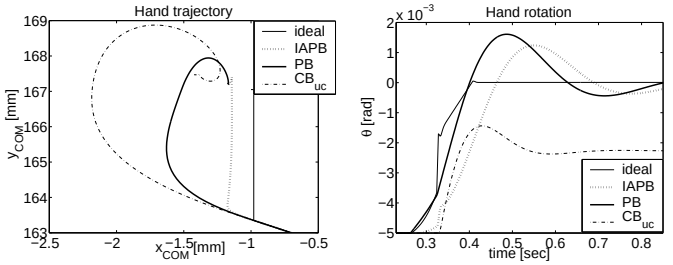

(a) (b)

Fig. 10. Simulated hand trajectories obtained when constraint-based ("ideal"), impulse-augmented penalty-based ("IAPB"), and penalty-based ("PB") interactions are transmitted to users by a four channel controller, and when constraint-based interactions are transmitted to users by a unilateral coupler ("CB_{uc}"). Collision impulses computed using the proposed method are spread over several simulation steps when necessary. Note that the hand trajectory is closest to the ideal trajectory during the interaction with a impulse-augmented penalty-based virtual world regardless of the limitations of the device.

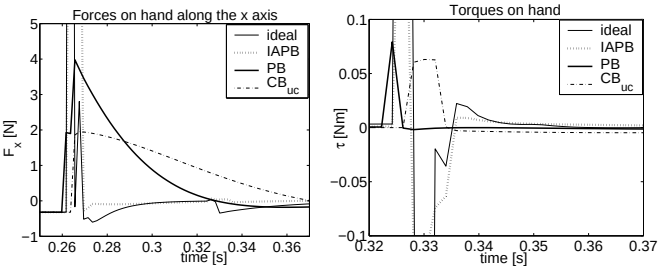

(a) (b)

Fig. 11. Simulated forces and torques applied to users by the four channel controller when the virtual world is generated using the constraint-based ("ideal"), the impulse-augmented penalty-based ("IAPB") and the penalty-based ("PB") methods, and applied by the unilateral coupler when the virtual environment is generated using the constraint-based method ("CB_{uc})". Collision impulses computed using the proposed technique are spread over several simulation steps when necessary. Note that, though limited, the forces applied to users upon collision are still larger than the penalty-based forces.

loss of performance due to limited force capabilities of the haptic interface is diminished most by spreading the collision impulses over several steps of the simulation. Therefore, this technique is used to overcome device force limitations in the following simulations and experiments.

Both scaling and spreading of collision impulses are equivalent to adapting the coefficient of restitution to the device capabilities. As a result of this adaptation, the effective coefficient of restitution may be negative and the post-collision normal contact velocities may be negative (i.e., bodies may move into each other after collision resolution). Nevertheless, the passivity of the proposed collision resolution method is not affected by an adaptive coefficient of restitution. (24) shows that the post-collision kinetic energy of the system is at most equal to its pre-collision kinetic energy for any $e \in [-1, 1]$. Hence, adapting the coefficient of restitution to the device capabilities does not influence the stability of the haptic interaction.

As the force capabilities of the haptic interface decrease, the haptic and visual performance of the proposed approach diminishes. For $e = -1$, the impulse-augmented penalty-based simulation reduces to a penalty-based simulation. The haptic performance reduction can be seen by comparing Figures 10 and 7. In Figure 10, it is assumed that the device can apply at most $\boldsymbol{F}_{limit} = \begin{pmatrix} 15\mathrm{N} & 15\mathrm{N} & 1\mathrm{Nm} \end{pmatrix}^T$ and collision impulses are spread over more time steps when necessary. In Figure 7, it is assumed that the device can fully apply the collision impulses to the user's hand. The hand trajectories representing interactions with the impulse-augmented penalty-based and penalties-only virtual environments are closer to each other in Figure 10 than they are in Figure 7. The visual performance diminishes correspondingly, as the virtual tool penetrates the constraints deeper when spreading is required than when the device can fully apply the collision impulses. Nevertheless, constraint penetration is smaller in the proposed simulation than in the penalty-based one regardless of the device limitations. Both the haptic and the visual performance of the impulse-augmented penalty-based virtual world is better than that of the penalty-based world. In addition, the perceptual advantage obtained by applying abrupt forces to the user's hand upon contact is maintained, since the forces and torques felt by users are larger when they interact with the proposed simulation than when they interact with the penalty-based one (see Figure 11).

VII. Experiments

In this section, the performance of the proposed approach is evaluated against that of the penalty-based approach through experiments carried out on a virtual environment system developed in the Robotics and Control Laboratory at the University of British Columbia. The evaluation is performed using the same controlled interaction and the same system setup as in Section VI. Therefore, the forces felt by users during experiments can be compared to those predicted through

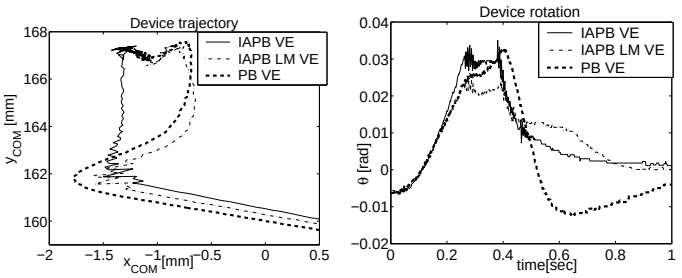

(a) (b)

Fig. 12. Experimental device trajectories during controlled interaction with impulse-augmented penalty-based and penalty virtual worlds ("IAPB" - impulse-augmented penalty-based world, full collision impulses applied to the device; "IAPB LM" - impulse-augmented penalty-based world, limited collision impulses applied to the device; "PB" - penalty world). Note that the peg bounces less and settles into the corner faster when the virtual world is generated using the proposed approach.

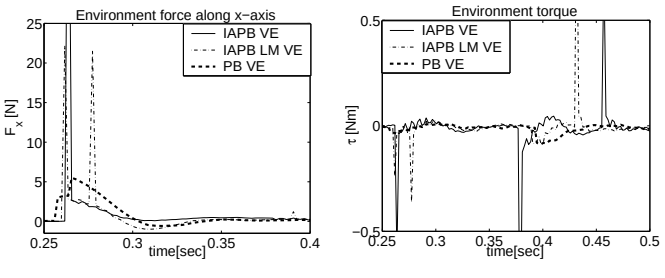

(a) (b)

Fig. 13. Forces and torques applied to the device during controlled interaction with impulse-augmented penalty-based and penalty virtual worlds ("IAPB" - impulse-augmented penalty-based world, full collision impulses applied to the device; "IAPB LM" - impulse-augmented penalty-based world, limited collision impulses applied to the device; "PB" - penalty world). Note the large impulses upon collision and the faster settling of the peg into the corner during the interaction with the proposed world.

simulations. The system comprises a planar haptic interface, a testbed virtual environment, a controller that coordinates both forces and positions between the haptic interface and the virtual environment, and a graphical display. Hand forces are not directly measurable. They are computed using a system state observer, the accurate dynamic model of the device, as well as the measured joint angles and applied actuator torques, as detailed in [34]. A 700MHz Pentium III personal computer running VxWorks is used to implement the virtual world simulation and the device and coordination controllers at a haptic sampling rate of 512Hz. A Pentium IV personal computer running Windows 2000 displays the virtual environment using information received from the haptics engine via a UDP connection at an average rate of 30Hz.

To ensure the same initial conditions and the same "user" during all experiments, the user's hand is replaced with a constant force (Figure 4). Since the haptic device is an impedance-type interface, elimination of the adaptive hand damping represents a worst case for stability. Figures 12 and 13 present the results obtained when the virtual environment is generated using both a penalty and the proposed simulation.

Figure 12 demonstrates increased contact stability in the impulse-augmented penalty-based virtual world compared to the penalty-based one. The peg settles into the corner faster and bounces less when collision impulses are applied to the device. As shown in [20], the impulsive "braking" forces amount to increasing the damping gain in the device to a very large value only upon penetration into the constraint. Sustained damping of equivalent gain while the interface is within the constraint would cause the system to be stable. Hence, a stiff implementation of a rigid corner augmented with impulsive forces upon constraint penetration improves performance because it generates a trajectory that is closer to the trajectory imposed by a real rigid corner. Alternatively, a conventional stiff implementation of a rigid corner would approach the ideal trajectory only through increased gains. This would result in a lower stability margin.

As expected, the performance of the impulse-augmented penalty-based world decreases when collision impulses are applied over several steps in order to meet the device rendering capabilities (the maximum force that the device can apply is chosen to be $\boldsymbol{F}_{limit} = \begin{pmatrix} 15\text{N} & 15\text{N} & 1\text{Nm} \end{pmatrix}^T$ for this experiment). A device that can apply only limited forces and torques dissipates less energy upon impact than that predicted by the chosen coefficient of restitution. However, it dissipates more energy than during penalty-based interaction. Moreover, the perceptual advantage of large force transitions upon contact is maintained. Though limited, the impulsive forces rendered to the user are much larger than the penalty-based contact forces (see Figure 13).

Increased virtual wall damping would also result in larger force transitions upon impact and less bouncing, i.e., more stable contact. However, the virtual damping is limited by the physical damping, the virtual wall stiffness, and the simulation step during 1 DOF interaction with a virtual wall [7]. The virtual damping may also be limited by geometry during rigid body interaction. Guidelines for choosing it without causing instability are not available presently. Hence, only limited improvements in the perceived rigidity of the virtual contacts could be achieved through increasing the virtual damping if the virtual wall stiffness is large (as needed for a convincingly rigid resting contacts) and the physical damping is small (as needed for imperceptible device dynamics). On the other hand, the impulsive forces provide a physically-based technique for enhancing the realism of the interaction that does not increase the kinetic energy of the simulated environment and is limited only by the device capabilities.

The controlled experiment presented in this section demonstrates the increased stability and perceived rigidity of impulse-augmented penalty-based rigid body contacts compared to penalty-based rigid body contacts. Nonetheless, the example interaction is simple and does not illustrate the computational performance of the proposed approach during spatial (6 DOF) rigid body interactions. In this example, at most six collisions have been resolved simultaneously (they occur when the user inserts the peg into the tight fitting hole at the top of the

virtual world depicted in Figure 4) and collision resolution has not been a limiting factor[5]. Therefore, intensive further tests are needed to validate the feasibility of the approach for 6 DOF manipulations in cluttered virtual environments. These tests must illustrate whether the pseudo-inversion of the square matrix $\mathcal{J}_c \boldsymbol{D}^{-1} \mathcal{J}_c^T$ meets the speed required by the haptic controller during interactions involving a large number of simultaneous collisions.

VIII. Conclusions

The simulation approach proposed in this paper improves the stability and the perceived rigidity of contacts during haptic interaction with multi rigid body virtual worlds. The approach is based on a new model of rigid body contact that assumes infinite stiffness upon contact and limited stiffness during contact. The infinite stiffness upon contact is rendered to users through impulsive forces, while the limited stiffness during contact is rendered through penalty forces. The impulsive forces are computed using a new simultaneous collision resolution method that never increases the kinetic energy of the multi rigid body virtual world. When new contacts arise, the impulsive forces generate large hand accelerations without requiring increased contact stiffness and damping. The performance of the proposed approach is compared with that of existing haptic methods for virtual environment generation. Simulations and controlled experiments demonstrate improved contact stability in a planar virtual world.

Future work will investigate the numerical performance of the proposed collision resolution method during spatial (6 DOF) rigid body manipulations. Extensions of the method to simultaneous impacts with different coefficients of restitution and the incorporation of dry friction in the collision response will also be studied. To enable users to distinguish interactions with objects made of various materials, alternative impulse rendering techniques will be explored. These extensions will increase the realism of the impulsive interaction with an impulse-augmented penalty-based virtual environment.

Appendix I
Passivity of the collision map for one collision

This section presents the proof of Theorem 1. *Proof:* The proof starts by computing the contact impulse by substitution of (15) into (9):

$$\begin{aligned} -e\mathcal{J}_c\dot{\boldsymbol{q}}_0 &= \mathcal{J}_c\dot{\boldsymbol{q}}_0 + \mathcal{J}_c\boldsymbol{D}^{-1}\mathcal{J}_c^T\boldsymbol{p} \Rightarrow \\ \boldsymbol{p} &= -(1+e)\left(\mathcal{J}_c\boldsymbol{D}^{-1}\mathcal{J}_c^T\right)^{-1}\mathcal{J}_c\dot{\boldsymbol{q}}_0. \end{aligned} \quad (27)$$

Then, the post-collision configuration space velocity results after substitution from (27) in (9):

$$\begin{aligned} \dot{\boldsymbol{q}} &= \dot{\boldsymbol{q}}_0 - (1+e)\boldsymbol{D}^{-1}\mathcal{J}_c^T\left(\mathcal{J}_c\boldsymbol{D}^{-1}\mathcal{J}_c^T\right)^{-1}\mathcal{J}_c\dot{\boldsymbol{q}}_0 = \\ &= \left(\boldsymbol{I} - (1+e)\overline{\mathcal{J}}_c\mathcal{J}_c\right)\dot{\boldsymbol{q}}_0 \end{aligned} \quad (28)$$

[5]Neither was collision resolution a limiting factor during the experiments described in [4]. In these experiments, a planar linkage with three links and revolute joints is manipulated in a virtual environment including a rigid enclosure and two other moving objects. Linkage operation is illustrated for both perfectly elastic and perfectly plastic contacts.

where $\boldsymbol{I}$ is the $d \times d$ identity matrix.

Next it is shown that:

$$\boldsymbol{D}\overline{\mathcal{J}}_c\mathcal{J}_c - \mathcal{J}_c^T\overline{\mathcal{J}}_c^T\boldsymbol{D}\overline{\mathcal{J}}_c\mathcal{J}_c = 0. \quad (29)$$

Indeed, using the definition of the dynamically consistent inverse of $\mathcal{J}_c$ and the symmetry of the inertia matrix:

$$\begin{aligned} &\boldsymbol{D}\overline{\mathcal{J}}_c\mathcal{J}_c - \mathcal{J}_c^T\overline{\mathcal{J}}_c^T\boldsymbol{D}\overline{\mathcal{J}}_c\mathcal{J}_c = \\ &= \boldsymbol{D}\boldsymbol{D}^{-1}\mathcal{J}_c^T\left(\mathcal{J}_c\boldsymbol{D}^{-1}\mathcal{J}_c^T\right)^{-1}\mathcal{J}_c - \\ &\quad \mathcal{J}_c^T\left(\boldsymbol{D}^{-1}\mathcal{J}_c^T\left(\mathcal{J}_c\boldsymbol{D}^{-1}\mathcal{J}_c^T\right)^{-1}\right)^T\boldsymbol{D}\boldsymbol{D}^{-1} \\ &\quad \mathcal{J}_c^T\left(\mathcal{J}_c\boldsymbol{D}^{-1}\mathcal{J}_c^T\right)^{-1}\mathcal{J}_c = \\ &= \mathcal{J}_c^T\left(\mathcal{J}_c\boldsymbol{D}^{-1}\mathcal{J}_c^T\right)^{-1}\mathcal{J}_c - \mathcal{J}_c^T\left(\mathcal{J}_c\boldsymbol{D}^{-1}\mathcal{J}_c^T\right)^{-T} \\ &\quad \mathcal{J}_c\boldsymbol{D}^{-T}\mathcal{J}_c^T\left(\mathcal{J}_c\boldsymbol{D}^{-1}\mathcal{J}_c^T\right)^{-1}\mathcal{J}_c = \\ &= \mathcal{J}_c^T\left(\mathcal{J}_c\boldsymbol{D}^{-1}\mathcal{J}_c^T\right)^{-1}\mathcal{J}_c - \mathcal{J}_c^T\left(\mathcal{J}_c\boldsymbol{D}^{-1}\mathcal{J}_c^T\right)^{-1} \\ &\quad \mathcal{J}_c\boldsymbol{D}^{-1}\mathcal{J}_c^T\left(\mathcal{J}_c\boldsymbol{D}^{-1}\mathcal{J}_c^T\right)^{-1}\mathcal{J}_c = 0. \end{aligned} \quad (30)$$

In (30), $\left(\mathcal{J}_c\boldsymbol{D}^{-1}\mathcal{J}_c^T\right)^{-T} = \left(\mathcal{J}_c\boldsymbol{D}^{-1}\mathcal{J}_c^T\right)^{-1}$ and $\boldsymbol{D}^{-T} = \boldsymbol{D}^{-1}$ since they are symmetric. Furthermore:

$$\begin{aligned} &\left(\boldsymbol{D}\overline{\mathcal{J}}_c\mathcal{J}_c - \mathcal{J}_c^T\overline{\mathcal{J}}_c^T\boldsymbol{D}\overline{\mathcal{J}}_c\mathcal{J}_c\right)^T = \\ &= \mathcal{J}_c^T\overline{\mathcal{J}}_c^T\boldsymbol{D} - \mathcal{J}_c^T\overline{\mathcal{J}}_c^T\boldsymbol{D}\overline{\mathcal{J}}_c\mathcal{J}_c = 0. \end{aligned} \quad (31)$$

Then, the post-collision kinetic energy of the system is be computed as follows:

$$\begin{aligned} &KE = \frac{1}{2}\dot{\boldsymbol{q}}^T\boldsymbol{D}\dot{\boldsymbol{q}} = \\ &= \frac{1}{2}\dot{\boldsymbol{q}}_0^T\left(\boldsymbol{I} - (1+e)\mathcal{J}_c^T\overline{\mathcal{J}}_c^T\right)\boldsymbol{D}\left(\boldsymbol{I} - (1+e)\overline{\mathcal{J}}_c\mathcal{J}_c\right)\dot{\boldsymbol{q}}_0 = \\ &= \frac{1}{2}\dot{\boldsymbol{q}}_0^T\boldsymbol{D}\dot{\boldsymbol{q}}_0 - (1+e)\frac{1}{2}\dot{\boldsymbol{q}}_0^T \\ &\quad \left(\boldsymbol{D}\overline{\mathcal{J}}_c\mathcal{J}_c + \mathcal{J}_c^T\overline{\mathcal{J}}_c^T\boldsymbol{D} - (1+e)\mathcal{J}_c^T\overline{\mathcal{J}}_c^T\boldsymbol{D}\overline{\mathcal{J}}_c\mathcal{J}_c\right)\dot{\boldsymbol{q}}_0 = \\ &= KE_0 - (1+e)\frac{1}{2}\dot{\boldsymbol{q}}_0^T \\ &\quad \left(2\mathcal{J}_c^T\overline{\mathcal{J}}_c^T\boldsymbol{D}\overline{\mathcal{J}}_c\mathcal{J}_c - (1+e)\mathcal{J}_c^T\overline{\mathcal{J}}_cT\boldsymbol{D}\overline{\mathcal{J}}_c\mathcal{J}_c\right)\dot{\boldsymbol{q}}_0 = \\ &= KE_0 - \left(1-e^2\right)\dot{\boldsymbol{q}}_0^T\mathcal{J}_c^T\overline{\mathcal{J}}_c^T\boldsymbol{D}\overline{\mathcal{J}}_c\mathcal{J}_c\dot{\boldsymbol{q}}_0. \end{aligned} \quad (32)$$

Since $\mathcal{J}_c^T\overline{\mathcal{J}}_c^T\boldsymbol{D}\overline{\mathcal{J}}_c\mathcal{J}_c$ is symmetric, it is positive semi-definite and

$$KE \leq KE_0 \quad \forall e \in [0,1]$$

■

Appendix II
Passivity of the collision map for overdetermined constraints

This section presents the proof of Theorem 2. *Proof:* The proof follows the same reasoning as the proof

of Theorem 1, where $\left(\boldsymbol{\mathcal{J}}_c\boldsymbol{D}^{-1}\boldsymbol{\mathcal{J}}_c^T\right)^{-1}$ is replaced by $\left(\boldsymbol{\mathcal{J}}_c\boldsymbol{D}^{-1}\boldsymbol{\mathcal{J}}_c^T\right)^{\dagger}$. The proof holds since

$$\left(\boldsymbol{\mathcal{J}}_c\boldsymbol{D}^{-1}\boldsymbol{\mathcal{J}}_c^T\right)^{\dagger}=\left(\boldsymbol{\mathcal{J}}_c\boldsymbol{D}^{-1}\boldsymbol{\mathcal{J}}_c^T\right)^{\dagger}\boldsymbol{\mathcal{J}}_c\boldsymbol{D}^{-1}\boldsymbol{\mathcal{J}}_c^T\left(\boldsymbol{\mathcal{J}}_c\boldsymbol{D}^{-1}\boldsymbol{\mathcal{J}}_c^T\right)^{\dagger}$$

.

Furthermore, it is shown in Appendix III that:

$$\boldsymbol{\mathcal{J}}_c^T\left(\boldsymbol{\mathcal{J}}_c\boldsymbol{D}^{-1}\boldsymbol{\mathcal{J}}_c^T\right)^{\dagger}\boldsymbol{\mathcal{J}}_c=\boldsymbol{\mathcal{J}}_n^T\left(\boldsymbol{\mathcal{J}}_n\boldsymbol{D}^{-1}\boldsymbol{\mathcal{J}}_n^T\right)^{-1}\boldsymbol{\mathcal{J}}_n, \quad (33)$$

where $\boldsymbol{\mathcal{J}}_c^T=\begin{bmatrix}\boldsymbol{\mathcal{J}}_n^T & \boldsymbol{\mathcal{J}}_r^T\end{bmatrix}^T$ and $\boldsymbol{\mathcal{J}}_n$ is full row rank. Then:

$$\begin{aligned}
&KE=KE_0-\left(1-e^2\right)\dot{\boldsymbol{q}}_0^T\boldsymbol{\mathcal{J}}_c^T\overline{\boldsymbol{\mathcal{J}}}_c^T\boldsymbol{D}\overline{\boldsymbol{\mathcal{J}}}_c\boldsymbol{\mathcal{J}}_c\dot{\boldsymbol{q}}_0=\\
&=KE_0-\left(1-e^2\right)\dot{\boldsymbol{q}}_0^T\boldsymbol{\mathcal{J}}_c^T\left(\boldsymbol{D}^{-1}\boldsymbol{\mathcal{J}}_c^T\left(\boldsymbol{\mathcal{J}}_c\boldsymbol{D}^{-1}\boldsymbol{\mathcal{J}}_c^T\right)^{\dagger}\right)^T\\
&\boldsymbol{D}\left(\boldsymbol{D}^{-1}\boldsymbol{\mathcal{J}}_c^T\left(\boldsymbol{\mathcal{J}}_c\boldsymbol{D}^{-1}\boldsymbol{\mathcal{J}}_c^T\right)^{\dagger}\right)\boldsymbol{\mathcal{J}}_c\dot{\boldsymbol{q}}_0=\\
&=KE_0-\left(1-e^2\right)\dot{\boldsymbol{q}}_0^T\boldsymbol{\mathcal{J}}_c^T\left(\boldsymbol{\mathcal{J}}_c\boldsymbol{D}^{-1}\boldsymbol{\mathcal{J}}_c^T\right)^{\dagger}\\
&\boldsymbol{\mathcal{J}}_c\boldsymbol{D}^{-1}\boldsymbol{\mathcal{J}}_c^T\left(\boldsymbol{\mathcal{J}}_c\boldsymbol{D}^{-1}\boldsymbol{\mathcal{J}}_c^T\right)^{\dagger}\boldsymbol{\mathcal{J}}_c\dot{\boldsymbol{q}}_0=\\
&=KE_0-\left(1-e^2\right)\dot{\boldsymbol{q}}_0^T\boldsymbol{\mathcal{J}}_c^T\left(\boldsymbol{\mathcal{J}}_c\boldsymbol{D}^{-1}\boldsymbol{\mathcal{J}}_c^T\right)^{\dagger}\boldsymbol{\mathcal{J}}_c\dot{\boldsymbol{q}}_0=\\
&=KE_0-\left(1-e^2\right)\dot{\boldsymbol{q}}_0^T\boldsymbol{\mathcal{J}}_n^T\overline{\boldsymbol{\mathcal{J}}}_n^T\boldsymbol{D}\overline{\boldsymbol{\mathcal{J}}}_n\boldsymbol{\mathcal{J}}_n\dot{\boldsymbol{q}}_0. \qquad (34)
\end{aligned}$$

Since $\boldsymbol{\mathcal{J}}_n^T\overline{\boldsymbol{\mathcal{J}}}_n^T\boldsymbol{D}\overline{\boldsymbol{\mathcal{J}}}_n\boldsymbol{\mathcal{J}}_n$ is positive semi-definite, simultaneous collision resolution is passive, i.e. $KE\leq KE_0 \quad \forall e\in[0,1]$, when the constraints are overdetermined. ■

APPENDIX III
PROOF OF IMPLICIT ELIMINATION OF CONSTRAINT OVERDETERMINANCY

Proof: This section proves that (33) holds by showing that:

- $\boldsymbol{\mathcal{J}}_c\boldsymbol{D}^{-1}\boldsymbol{\mathcal{J}}_c^T$ is invertible when $\boldsymbol{\mathcal{J}}_c$ is full row rank;
- $\boldsymbol{\mathcal{J}}_c^T\left(\boldsymbol{\mathcal{J}}_c\boldsymbol{D}^{-1}\boldsymbol{\mathcal{J}}_c^T\right)^{\dagger}\boldsymbol{\mathcal{J}}_c=\boldsymbol{\mathcal{J}}_n^T\left(\boldsymbol{\mathcal{J}}_n\boldsymbol{D}^{-1}\boldsymbol{\mathcal{J}}_n^T\right)^{-1}\boldsymbol{\mathcal{J}}_n$ when $\boldsymbol{\mathcal{J}}_c$ is row rank deficient, $\boldsymbol{\mathcal{J}}_n$ is full row rank, and $\boldsymbol{\mathcal{J}}_c^T=\begin{bmatrix}\boldsymbol{\mathcal{J}}_n^T & \boldsymbol{\mathcal{J}}_r^T\end{bmatrix}$.

If $\boldsymbol{\mathcal{J}}_c$ is full row rank, then the symmetric matrix $\boldsymbol{\mathcal{J}}_c\boldsymbol{\mathcal{J}}_c^T$ is invertible and all its singular values are strictly positive. Therefore:

$$\begin{aligned}
&\boldsymbol{v}^T\boldsymbol{\mathcal{J}}_c\boldsymbol{D}^{-1}\boldsymbol{\mathcal{J}}_c^T\boldsymbol{v}\geq\lambda_{min}\left(\boldsymbol{D}^{-1}\right)\boldsymbol{v}^T\boldsymbol{\mathcal{J}}_c\boldsymbol{\mathcal{J}}_c^T\boldsymbol{v}\geq\\
&\geq\lambda_{min}\left(\boldsymbol{D}^{-1}\right)\lambda_{min}\left(\boldsymbol{\mathcal{J}}_c\boldsymbol{\mathcal{J}}_c^T\right)\boldsymbol{v}\boldsymbol{v}^T>0 \quad \forall\boldsymbol{v}\neq\boldsymbol{0} \qquad (35)
\end{aligned}$$

i.e., $\boldsymbol{\mathcal{J}}_c\boldsymbol{D}^{-1}\boldsymbol{\mathcal{J}}_c^T$ is positive definite, hence invertible.

If $\boldsymbol{\mathcal{J}}_c$ is row rank deficient, let $\boldsymbol{\mathcal{J}}_c$ be given by $\boldsymbol{\mathcal{J}}_c^T=\begin{bmatrix}\boldsymbol{\mathcal{J}}_n^T & \boldsymbol{\mathcal{J}}_r^T\end{bmatrix}^T$, where $\boldsymbol{\mathcal{J}}_n$ is full row rank, i.e., $rank(\boldsymbol{\mathcal{J}}_n)=rank(\boldsymbol{\mathcal{J}}_c)=n$ and $rank(\boldsymbol{\mathcal{J}}_r)=r$. By elementary row operations:

$$\begin{bmatrix}\boldsymbol{I}_n & \boldsymbol{0}\\ \boldsymbol{A} & \boldsymbol{I}_r\end{bmatrix}\begin{bmatrix}\boldsymbol{\mathcal{J}}_n\\ \boldsymbol{\mathcal{J}}_r\end{bmatrix}=\begin{bmatrix}\boldsymbol{\mathcal{J}}_n\\ \boldsymbol{0}\end{bmatrix}, \qquad (36)$$

where $\boldsymbol{A}\in\mathcal{R}^{r\times n}$ and $\boldsymbol{I}_n$ and $\boldsymbol{I}_r$ are identity matrices of rank n and r, respectively.

Then:

$$\begin{aligned}
&\left(\boldsymbol{\mathcal{J}}_c\boldsymbol{D}^{-1}\boldsymbol{\mathcal{J}}_c^T\right)^{\dagger}=\\
&=\left(\begin{bmatrix}\boldsymbol{I}_n & \boldsymbol{0}\\ \boldsymbol{A} & \boldsymbol{I}_r\end{bmatrix}^{-1}\begin{bmatrix}\boldsymbol{\mathcal{J}}_n\\ \boldsymbol{0}\end{bmatrix}\boldsymbol{D}^{-1}\begin{bmatrix}\boldsymbol{\mathcal{J}}_n^T & \boldsymbol{0}^T\end{bmatrix}\begin{bmatrix}\boldsymbol{I}_n & \boldsymbol{A}^T\\ \boldsymbol{0} & \boldsymbol{I}_r\end{bmatrix}^{-T}\right)^{\dagger}=\\
&=\left(\begin{bmatrix}\boldsymbol{I}_n & \boldsymbol{0}\\ -\boldsymbol{A} & \boldsymbol{I}_r\end{bmatrix}\begin{bmatrix}\boldsymbol{\mathcal{J}}_n\\ \boldsymbol{0}\end{bmatrix}\boldsymbol{D}^{-1}\begin{bmatrix}\boldsymbol{\mathcal{J}}_n^T & \boldsymbol{0}^T\end{bmatrix}\begin{bmatrix}\boldsymbol{I}_n & -\boldsymbol{A}^T\\ \boldsymbol{0} & \boldsymbol{I}_r\end{bmatrix}\right)^{\dagger}=\\
&=\begin{bmatrix}\boldsymbol{I}_n & \boldsymbol{A}^T\\ \boldsymbol{0} & \boldsymbol{I}_r\end{bmatrix}\begin{bmatrix}\boldsymbol{\mathcal{J}}_n\boldsymbol{D}^{-1}\boldsymbol{\mathcal{J}}_n^T & \boldsymbol{0}\\ \boldsymbol{0} & \boldsymbol{0}\end{bmatrix}^{\dagger}\begin{bmatrix}\boldsymbol{I}_n & \boldsymbol{0}\\ \boldsymbol{A} & \boldsymbol{I}_r\end{bmatrix}. \qquad (37)
\end{aligned}$$

The last algebraic manipulation is based on the fact that:

$$\left(\boldsymbol{X}\boldsymbol{X}^T\right)^{\dagger}=\left(\boldsymbol{X}^T\right)^{\dagger}\boldsymbol{X}^{\dagger}. \qquad (38)$$

To show that (38) holds, let the SVD of $\boldsymbol{X}$ be given as $\boldsymbol{X}=\boldsymbol{U}\boldsymbol{\Sigma}\boldsymbol{V}^T$. Then:

$$\begin{aligned}
\left(\boldsymbol{X}\boldsymbol{X}^T\right)^{\dagger} &= \left(\boldsymbol{U}\boldsymbol{\Sigma}\boldsymbol{\Sigma}\boldsymbol{U}^T\right)^{\dagger}=\boldsymbol{U}\boldsymbol{\Sigma}'\boldsymbol{\Sigma}'\boldsymbol{U}^T=\\
&= \boldsymbol{U}\boldsymbol{\Sigma}'\boldsymbol{V}^T\boldsymbol{V}\boldsymbol{\Sigma}'\boldsymbol{U}^T=\left(\boldsymbol{X}^T\right)^{\dagger}\boldsymbol{X}^{\dagger}, \qquad (39)
\end{aligned}$$

where:

$$\boldsymbol{\Sigma}'=\begin{bmatrix}\frac{1}{\sigma_1} & \cdots & \cdots & \cdots & 0\\ \vdots & & & & \\ 0 & \cdots & \frac{1}{\sigma_n} & \cdots & 0\\ 0 & \cdots & 0 & \cdots & 0\end{bmatrix}, \qquad (40)$$

and $\sigma_1\cdots\sigma_n$ are the singular values of $\boldsymbol{X}$.

$\boldsymbol{\mathcal{J}}_c^T\left(\boldsymbol{\mathcal{J}}_c\boldsymbol{D}^{-1}\boldsymbol{\mathcal{J}}_c^T\right)^{\dagger}\boldsymbol{\mathcal{J}}_c$ can now be computed using (36) and (37):

$$\begin{aligned}
&\boldsymbol{\mathcal{J}}_c^T\left(\boldsymbol{\mathcal{J}}_c\boldsymbol{D}^{-1}\boldsymbol{\mathcal{J}}_c^T\right)^{\dagger}\boldsymbol{\mathcal{J}}_c=\\
&=\boldsymbol{\mathcal{J}}_c^T\begin{bmatrix}\boldsymbol{I}_n & \boldsymbol{A}^T\\ \boldsymbol{0} & \boldsymbol{I}_r\end{bmatrix}\begin{bmatrix}\boldsymbol{\mathcal{J}}_n\boldsymbol{D}^{-1}\boldsymbol{\mathcal{J}}_n^T & \boldsymbol{0}\\ \boldsymbol{0} & \boldsymbol{0}\end{bmatrix}^{\dagger}\begin{bmatrix}\boldsymbol{I}_n & \boldsymbol{0}\\ \boldsymbol{A} & \boldsymbol{I}_r\end{bmatrix}\boldsymbol{\mathcal{J}}_c=\\
&=\begin{bmatrix}\boldsymbol{\mathcal{J}}_n^T & \boldsymbol{0}\end{bmatrix}\begin{bmatrix}\left(\boldsymbol{\mathcal{J}}_n\boldsymbol{D}^{-1}\boldsymbol{\mathcal{J}}_n^T\right)^{-1} & \boldsymbol{0}\\ \boldsymbol{0} & \boldsymbol{0}\end{bmatrix}\begin{bmatrix}\boldsymbol{\mathcal{J}}_n\\ \boldsymbol{0}\end{bmatrix}=\\
&=\boldsymbol{\mathcal{J}}_n^T\left(\boldsymbol{\mathcal{J}}_n\boldsymbol{D}^{-1}\boldsymbol{\mathcal{J}}_n^T\right)^{-1}\boldsymbol{\mathcal{J}}_n. \qquad (41)
\end{aligned}$$

■

REFERENCES

[1] L. Rosenberg and B. Adelstein, "Perceptual Decomposition of Virtual Haptic Surfaces," in *Proc IEEE Symp Res Front Virt Real*, Los Alamitos CA, 1993, pp. 46–53.

[2] D. Lawrence, L. Pao, A. Dougherty, M. Salada, and Y. Pavlou, "Rate-Hardness: A New Performance Metric for Haptic Interfaces," *IEEE T Robot Autom*, vol. 16, no. 4, pp. 357–371, 2000.

[3] D. Constantinescu, S. Salcudean, and E. Croft, "Haptic Rendering of Rigid Body Collisions," in *Proc 12 Int Symp Haptic Interf Virt Envir Teleop Syst*, Chicago, IL, 2004, pp. 1–6.

[4] ——, "Impulsive Forces for Haptic Rendering of Rigid Contacts," in *Proc 35 Int Symp Robot*, Paris, France, 2004, pp. 1–6.

[5] M. Moore and J. Wilhelms, "Collision Detection and Response for Computer Animation," *Comp Graphics (Proc ACM SIGGRAPH Conf)*, vol. 22, pp. 289–298, 1988.

[6] A. Gregory, A. Mascarenhas, S. Ehmann, M. Lin, and D. Manocha, "Six Degree-of-Freedom Haptic Display of Polygonal Models," in *IEEE Proc Visual*, 2000, pp. 139–146.

[7] J. Colgate and G. Schenkel, "Passivity of a Class of Sampled-Data Systems: Application to Haptic Interfaces," *J Robot Syst*, vol. 14, no. 1, pp. 37–47, 1997.
[8] D. Baraff, "Issues in Computing Contact Forces for Non-Penetrating Rigid Bodies," *Algorithmica*, vol. 10, no. 2-4, pp. 292–352, 1993.
[9] D. Ruspini and O. Khatib, "Collision/Contact Models for Dynamic Simulation and Haptic Interaction," in *Proc 9 Int Symp Robot Res*, Snowbird, UT, 1999, pp. 185–195.
[10] D. Stewart and J. Trinkle, "An Implicit Time-Stepping Scheme Rigid Body Dynamics with Inellastic Collisions and Coulomb Friction," *Int J Numer Method Eng*, vol. 39, no. 15, pp. 2673–2691, 1996.
[11] M. Anitescu and F. Potra, "Formulating dynamic multi-rigid-body contact problems with friction as solvable linear complementarity problems," *ASME Nonlinear Dynam*, vol. 14, pp. 231–247, 1997.
[12] M. Anitescu and G. Hart, "A Hard-Constraint Time-Stepping Approch for Rigid Multibody Dynamics with Joints, Contact, and Friction," in *Proc Conf Divers Comput*, Atlanta, GA, 2003, pp. 34–41.
[13] M. Cline and D. Pai, "Stabilization for Rigid Body Simulation with Contact and Constraints," in *Proc IEEE Int Conf Robot Autom*, Taipei, Taiwan, September 2003, pp. 3744–3751.
[14] M. Anitescu and G. Hart, "A Constraint-Stabilized Time-Stepping Approach for Rigid Multibody Dynamics with Joints, Contact and Friction," *Int J Numer Method Eng*, in press 2004.
[15] C. Zilles and J. Salisbury, "A Constraint-based God Object Method for Haptic Display," in *ASME Haptic Interf Virt Envir Teleop Syst*, Chicago, IL, 1994, pp. 146–150.
[16] D. Ruspini, K. Koralov, and O. Khatib, "The Haptic Display of Complex Graphical Environments," in *Proc SIGGRAPH 97*, Los Angeles, CA, 1997, pp. 345–352.
[17] D. Ruspini and O. Khatib, "Dynamic Models for Haptic Rendering Systems," in *Advances in Robot Kinematics: ARK98*, Strobl/Salzburg, Austria, 1998, pp. 523–532.
[18] B. Mirtich and J. Canny, "Impulse-based Dynamic Simulation," in *Workshop on Algorithmic Foundations of Robotics*, K. Goldberg, P. Halperin, J.-C. Latombe, and R. Wilson, Eds. A.K.Peters, Boston, MA., 1994, pp. 407–418.
[19] B. Chang and J. Colgate, "Real-Time Impulse-Based Simulation of Rigid Body Systems for Haptic Display," in *Proc ASME Int Mech Eng Congr Exhib*, Dallas, Texas, 1997, pp. 1–8.
[20] S. Salcudean and T. Vlaar, "On the Emulation of Stiff Walls and Static Friction with a Magnetically Levitated Input/Output Device," *J Dyn Syst-T ASME*, vol. 119, pp. 127–132, March 1997.
[21] D. Constantinescu, I. Chau, L. Filipozzi, S. DiMaio, and S. Salcudean, "Haptic Rendering of Planar Rigid-Body Motion using a Redundant Parallel Mechanism," in *Proc IEEE Int Conf Robot Autom*, Berkeley, Ca, 2000, pp. 2440–2445.
[22] D. Constantinescu, S. Salcudean, and E. Croft, "Haptic Feedback using Local Models of Interaction," in *Proc 11 Int Symp Haptic Interf Virt Envir Teleop Syst*, Los Angeles, Ca, 2003, pp. 416–421.
[23] B. Brogliato, *Nonsmooth Mechanics, Second Edition*. Springer-Verlag, London, 1999.
[24] J. Moreau, "Unilateral Contact and Dry Friction in Finite Freedom Dynamics," in *Nonsmooth Mechanics and Applications. CISM Courses and Lectures*, J. Moreau and P. Panagiotopoulos, Eds. International Centre for Mechanical Sciences, Springer-Verlag, 1988, vol. 302, pp. 1–82.
[25] F. Pffeifer and C. Glocker, *Multibody Dynamics with Unilateral Contacts*. Wiley, New York, 1996.
[26] J. D. Hwang, M. D. Williams, and G. Niemeyer, "Toward Event-Based Haptics: Rendering Contact Using Open-Loop Force Pulses," in *Proc 12 Int Symp Haptic Interf Virt Envir Teleop Syst*, Chicago, IL, March 2004, pp. 14–21.
[27] Y. Kim, M. Otaduy, M. Lin, and D. Manocha, "Six-Degree-of Freedom Haptic Display Using Localized Contact Computations," *Presence-Teleop Virt*, vol. 12, no. 3, pp. 277–295, June 2003.
[28] D. Redon, A. Kheddar, and S. Coquillart, "Gauss' Least Constraints Principle and Rigid Body Simulations," in *Proc IEEE Int Conf Robot Autom*, Washington, DC, 2002, pp. 517–522.
[29] A. Witkin and D. Baraff, "Physically Based Modeling: Principles and Practice. SIGGRAPH '97 Course Notes." [Online]. Available: http://www-2.cs.cmu.edu/afs/cs.cmu.edu/user/baraff/www/sigcourse/
[30] A. Nahvi, J. Hollerbach, R. Freier, and D. Nelson, "Display of Friction in Virtual Environments based on Human Finger Pad Characteristics," in *Proc ASME Dynam Syst Contr Div*, vol. DSC-64, 1998, pp. 179–184.
[31] V. Hayward and B. Armstrong, "A new computational model of friction applied to haptic rendering," in *"Experimental Robotics VI". Lect Notes Contr Inf*, P. Corke and J. Trevelyan, Eds. Springer-Verlag, 2000, vol. 250, pp. 403–412.
[32] I. Han and B. Gilmore, "Impact Analysis for Multiple Body Systems with Friction and Sliding Contact," *J Mech Des-T ASME*, vol. 115, pp. 412–422, September 1993.
[33] O. Khatib, "Inertial Properties in Robotic Manipulation: An Object-Level Framework," *Int J Robot Res*, vol. 13, no. 1, pp. 19–36, 1995.
[34] M. Sirouspour, S. DiMaio, S. Salcudean, P. Abolmaesumi, and C. Jones, "Haptic Interface Control – Design Issues and Experiments with a Planar Device," in *Proc 2000 IEEE Int Conf Robot Autom*, San Francisco, Ca, 2000, pp. 789–794.
[35] B. Hannaford and R. Anderson, "Experimental and Simulation Studies of Hard Contact Force Reflecting Teleoperation," in *Proc IEEE Int Conf Robot Autom*, Scottsdale, AZ, May 1988, pp. 24–29.